Fabrication of Microscale Polymeric Wavy and Coiling Structures via Side-Electrode-Assisted Near-Field Electrospinning: Modeling and Experiments

Xiangyu You
Department of Mechanical and Automation Engineering,
The Chinese University of Hong Kong,
Shatin 999077, Hong Kong
e-mail: xyyou@mae.cuhk.edu.hk

Yang Yang
Department of Mechanical and Automation Engineering,
The Chinese University of Hong Kong,
Shatin 999077, Hong Kong
e-mail: yyang2@mae.cuhk.edu.hk

Ping Guo[1]
Mem. ASME
Department of Mechanical Engineering,
Northwestern University,
2145 Sheridan Road, Evanston, IL 60208
e-mail: ping.guo@northwestern.edu

It is challenging for the existing fabrication strategies to generate microscale wavy and coiling structures with low cost and high efficiency. In this work, we develop a novel and simple method that allows the fabrication of microscale wavy and coiling fiber arrays via near-field electrospinning (NFES). In addition to the main vertical electric potential for polymer jet generation, additional electrostatic signals are applied to the side-auxiliary electrodes to dynamically control the fiber deposition. Compared with traditional electrospinning based on the buckling instability or mechanical collector movement, the proposed method shows advantages in terms of the controllability, stability, accuracy, and minimal feature size. A theoretical model to describe the polymer jet behaviors has been proposed to simulate the fabrication process by considering the momentum balance of viscoelastic, charge repulsive, and electric forces. The model has been directly verified through the comparison with experimental results. The effects of different process parameters on the fiber deposition patterns are analyzed and discussed. The processing capability has been further demonstrated by fabricating two-dimensional wavy and coiling patterns as well as three-dimensional wavy structures with the radius of curvature less than 100 µm.
[DOI: 10.1115/1.4046861]

Keywords: near-field electrospinning, auxiliary electrode, fiber deposition, wavy and coiling structures, micro- and nano-machining and processing, modeling and simulation

Introduction

Due to the unique characteristics and applications in the field of photovoltaic devices [1], sensors [2,3], actuators [4], electromagnetic devices [5,6], and stretchable electronics [7,8], microscale wavy/coiling structures have attracted a great deal of attention in the recent decade. Many processing techniques, including focused ion beam (FIB) machining [9], chemical vapor deposition (CVD) [10], micro-stereolithography (MSL) [11,12], have been developed to fabricate this form of structure. However, to generate wavy/coiling structures at the microscale, specialized equipment and tedious processes must be employed, which makes the fabrication process time-consuming and cost-intensive.

Near-field electrospinning (NFES), a technique that uses a large potential difference to form a liquid jet, is an efficient and simple method to fabricate microscale fibers. A large variety of materials have been successfully used in the electrospinning process, such as polymers, liquid metals, composites, and ceramics [13,14]. Compared with the traditional electrospinning process, NFES has its own advantages in fabricating orderly aligned fibers. In an NFES process, the nozzle-to-collector distance is reduced from several centimeters to a few millimeters, while the applied voltage is consequently decreased from tens of thousands of volts to several hundred volts. Due to the shortened nozzle-to-collector distance and the decreased applied voltage, the repulsive forces between the charged elements along the electrospinning jet are significantly reduced, thus eliminating the bending instability. Another main difference is the movement of the collector. In an NFES process, the collector is controlled to move in a user-defined trajectory; while in a traditional electrospinning process, the collector is usually kept stationary.

The buckling instability in NEFS is closely dependent on the relationship between the fiber deposition speed (FDS) and the collector translation speed (CTS). If the CTS is set equal or larger than the FDS, a tensile force will occur along the electrospinning jet, which balances the compressive stress to eliminate the buckling instability. If the CTS is set lower than the FDS, the longitudinal compressive force acting on the electrospinning jet cannot be balanced, which causes the buckling. Based on this principle, previous research has adopted two kinds of strategies to fabricate wavy or coiling structures: (i) to utilize the buckling instability to generate wavy or coiling patterns and (ii) to avoid the buckling instability and to fabricate the patterns via direct mechanical movement of the collector. Hellmann et al. [15] reported the experimental results with coiling patterns using the first approach, which was modified from a buckling-instability-based NFES process. Different kinds of structures with coiling patterns such as figure-of-eight, slanted-loop, and lapped-loop were demonstrated. However, the formation and morphology of the deposited fibers were largely determined by process conditions such as material properties, process parameters, and environment factors. The structures were fabricated in a passive way. Specifically, it is not possible to modify the pattern geometry in a controllable manner. Wu et al. [16] developed a crimped fiber writing process using the second approach via the mechanical collector movement. Through tuning the collector dwell time and movement direction, controllable and

---

regular crimped fibers were obtained. However, the diameter of the fabricated fibers was on the scale of several millimeters. If the fiber diameter was tuned to a small diameter (less than 10 micrometers), extremely high CTS (usually more than 100 mm/s) was required to balance the FDS. The mechanical stage was usually restricted to simple reciprocal motion in such high-speed conditions, which limits the deposition of complex patterns and the minimal achievable feature size.

In addition to the dynamic-mechanical-collection-based method, electric field manipulation has also been exploited to generate orderly deposited patterns from electrospinning. Several works have been done to control the deposition of fibers using electric field manipulation [17–21]. For instance, Li et al. [17] used a collector composed of two conductive strips separated by an insulating gap to generate uniaxially aligned fiber arrays. Qin et al. [21] used current-pulse-modulated electrohydrodynamic jet printing to achieve reliable silver tracks. Deitzel et al. [22] studied the feasibility of dampening the chaotic instability and controlling the fiber deposition by using an electrostatic lens element. However, these works are limited to the control of electrospinning jet to deposit in one dimension or to suppress the chaotic whipping mode to some extent. The precise control of a single electrospinning fiber for complex patterns is still a challenging task. The difficulties lie in the theoretical understanding of jet behavior under a time-variant electric field distribution. In a traditional electrospinning process, the electric field distribution is uniform and time-invariant, jet behavior can be theoretically predicted [23–26]. The Maxwell model [27,28] is one of the classic models to describe the dynamic process of the electrospinning jet. All the previous works were focused on the bending behavior of the charged jet with uniform electric field distribution in far-field electrospinning processes. However, under the influence of active control of the electric field, the field distribution becomes non-uniform and time-variant. The variation of the electric potential will oscillate the charged jet to introduce more complicated dynamics. The theoretical analysis of the jet behavior in NEFS under the influence of a non-uniform and dynamic electric field has not been attempted in the literature, which motivates this work.

In this paper, a new fabrication technique for arbitrary wavy and coiling microscale patterns is proposed by introducing active electrostatic signals to four-side-auxiliary electrodes in an NEFS setup. It has the potential to provide much higher operation bandwidth and accuracy to precisely control the fiber deposition dynamically. A theoretical model of jet trajectory is first constructed by considering the corresponding forces acting on the electrospinning jet including viscoelastic, charge repulsive, and electric forces. The model is verified through a set of experiments by comparing the simulation and experimental results. The effects of process parameters on the deposited pattern geometry are then analyzed. At last, the process capability is further demonstrated by fabricating various microscale wavy and coiling structures.

Fabrication of Wavy and Coiling Patterns by Electric Field Manipulation

Here, we propose a novel method by controlling electrostatic signals applied on the side-auxiliary electrodes (AE) to fabricate wavy and coiling patterns in NFES. In this method, both the constant vertical electric field added on the nozzle and dynamic lateral electric field added on the auxiliary electrodes are applied, which induce the vertical and lateral driving forces of the charged polymer jet, respectively. Under the influence of vertical electric field, charges accumulate on the surface of the polymer droplet, causing a strong electrostatic force between the nozzle and collector and making the polymer eject toward the collector vertically. Under the influence of lateral electric field, a lateral electrostatic force is induced toward the charged jet and drives it to oscillate dynamically. In this way, the microscale transverse motion of the electrospinning jet is actively controlled by the external electric field by adjusting the electrostatic signals applied to the auxiliary electrodes. The concept is demonstrated in Fig. 1 showing the oscillation of the electrospinning jet. When a sinusoidal signal is added to the side electrode, the vibration of the jet is observed in the lateral direction as shown in Fig. 1(a). When the auxiliary electrostatic signal is turned off, the jet returns to a straight line as shown in Fig. 1(b). The results show the feasibility to use the auxiliary signals to actuate and control the jet for fabricating wavy and coiling fiber patterns.

The process schematics are further illustrated in Fig. 2. For the fabrication of wavy patterns, the electrostatic signals are applied to a pair of auxiliary electrodes (AE-1 and AE-3) shown in Fig. 2(a). Following the dynamic electrostatic force, the electrospinning jet oscillates in the Y-direction. Combined with the collector movement in the X-direction, wavy patterns can be generated with controllable amplitudes (A) and wavelengths (λ). When four auxiliary electrodes are added (AE-1 to AE-4) as shown in Fig. 2(b), the jet motion can be controlled in a two-dimensional space. For the fabrication of coiling patterns, four sinusoidal voltage signals are applied to four-side electrodes with a phase shift of 90 deg. Due to the coupled electrostatic force in the X- and Y-directions as well as the vertical voltage difference in the Z-direction, the electrospinning jet will follow a spiral trajectory. Thus, coiling patterns can be collected together with the collector movement along the X-direction. It should be noted that arbitrary signal forms can be applied to produce other complex patterns as well.

Theoretical Modeling

Model Description. In this research, a theoretical model adapted from Reneker et al.'s work [28] is constructed to analyze the behavior of jet trajectory with non-uniform electric field distribution in the near-field electrospinning. The schematic drawing of the proposed theoretical model is shown in Fig. 3. The electrospinning
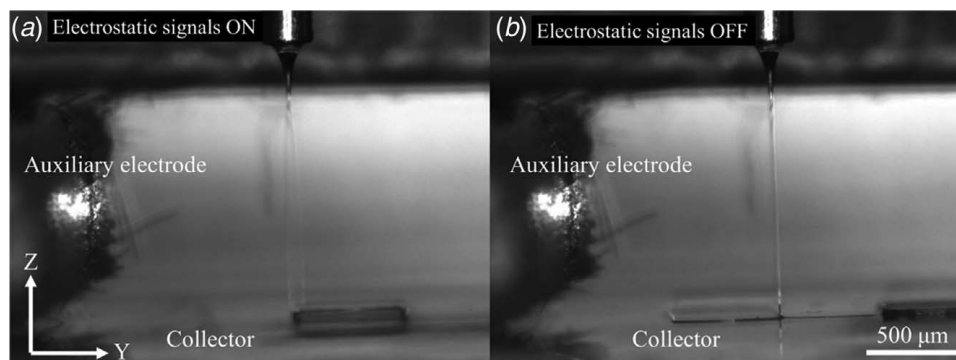
Fig. 1 Observations of the electrospinning jet (*a*) with and (*b*) without auxiliary electrostatic signals
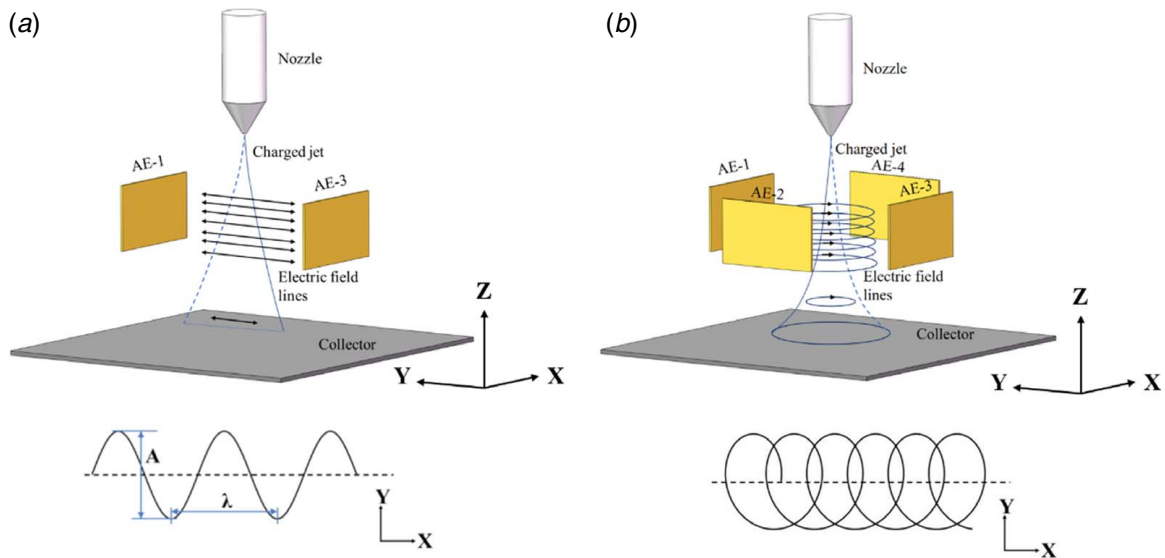
Fig. 2 Schematic illustration of the process to fabricate (a) wavy and (b) coiling structures
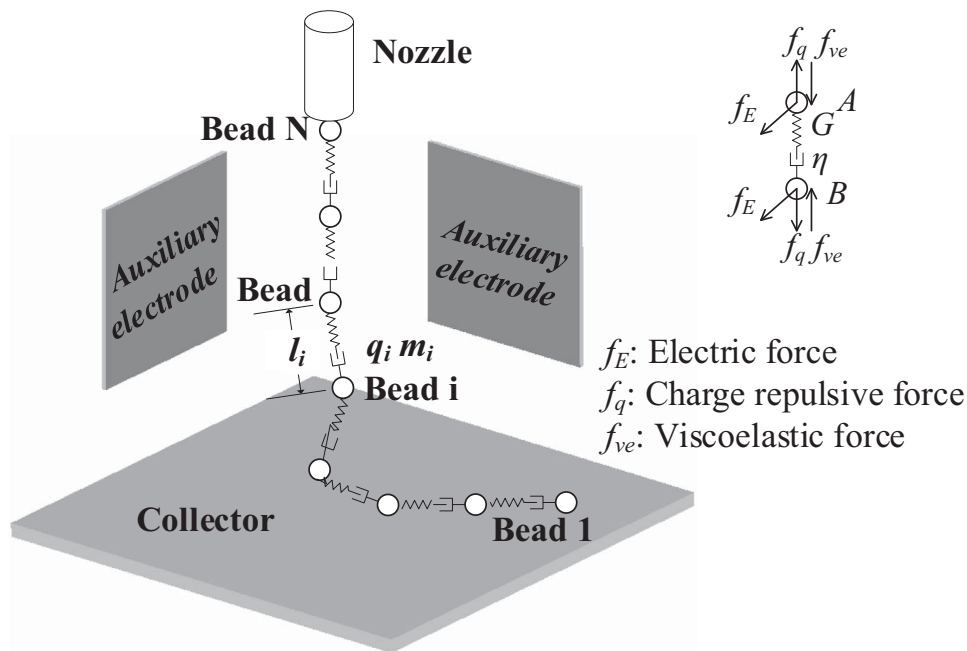
Fig. 3   Schematic of the theoretical model

jet is modeled as a series of charged beads connected via viscous dampers and elastic springs. Each bead is assumed to possess a charge q and mass m. The total number of beads is N. The forces acting on each bead are viscoelastic force, charge repulsive force, and electric force. Surface tension, aerodynamics, and gravity are negligibly small when compared with the other forces.

According to the continuity principle, when mass is conserved and evaporation is neglected, the jet radius a_i and jet segment length l_i of the ith bead have the relationship to the initial conditions as follows:

$$\pi a^2 l = \pi a_i^2 l_i^2 \tag{1}$$

In the Maxwell model, the viscoelastic stress between two adjacent beads is given as (σ is the viscoelastic stress, G is the

elastic modulus, and μ is the dynamic viscosity) [24]:

$$\frac{d\sigma_i}{dt} = G \frac{1}{l_i} \frac{dl_i}{dt} - \frac{G}{\mu} \sigma_i \tag{2}$$

For particular bead i, the viscoelastic forces act on both the prior bead ($i-1$) and the posterior bead ($i+1$) with the corresponding segment length l_i and l_{i+1}.

Then, the net viscoelastic force (f_{ve}) acting on the ith bead is

$$f_{ve} = \pi a_{i+1}^2 \sigma_{i+1} \left[i \frac{x_{i+1} - x_i}{l_{i+1}} + j \frac{y_{i+1} - y_i}{l_{i+1}} + k \frac{z_{i+1} - z_i}{l_{i+1}} \right] \\ - \pi a_i^2 \sigma_i \left[i \frac{x_i - x_{i-1}}{l_i} + j \frac{y_i - y_{i-1}}{l_i} + k \frac{z_i - z_{i-1}}{l_i} \right] \tag{3}$$

The charge repulsive force on bead i caused by another bead j is defined as $f_{q_{ij}}$ and given by (R_{ij} is the distance between the ith bead and the jth bead)

$$f_{q_{ij}} = \frac{q^2}{R_{ij}} \tag{4}$$

The total charge repulsive force (f_q) acting on the ith bead is the summation of Coulomb forces from every bead presented in the model along the jet, except for itself. The net charge repulsive force (f_q) acting on the ith bead is given by

$$F_q = \sum_{\substack{j=1,N \\ j \neq i}} \frac{q^2}{R_{ij}^2} \left[\boldsymbol{i} \frac{x_i - x_j}{R_{ij}} + \boldsymbol{j} \frac{y_i - y_j}{R_{ij}} + \boldsymbol{k} \frac{z_i - z_j}{R_{ij}} \right] \tag{5}$$

The electric force (f_E) acting on the ith bead created by the potential difference is:

$$F_E = -q \left(\boldsymbol{i} \frac{f_x}{h_x} + \boldsymbol{j} \frac{f_y}{h_y} + \boldsymbol{k} \frac{f_z}{h_z} \right) \tag{6}$$

where f_x, f_y, and f_z are electric forces along the X-axis, Y-axis, and Z-axis, respectively. h_x and h_y are the distance between the nozzle and the auxiliary-electrodes along the X-axis and Y-axis, respectively. h_z is the nozzle-to-collector distance.

According to Newton's second law, by setting the aforementioned force interactions in Eqs. (3), (5), and (6), the momentum balance of each individual bead is

$$m \frac{d^2(\boldsymbol{i}x_i + \boldsymbol{j}y_i + \boldsymbol{k}z_i)}{dt^2} = \pi a_{i+1}^2 \sigma_{i+1} \left[\boldsymbol{i} \frac{x_{i+1} - x_i}{l_{i+1}} + \boldsymbol{j} \frac{y_{i+1} - y_i}{l_{i+1}} + \boldsymbol{k} \frac{z_{i+1} - z_i}{l_{i+1}} \right]$$
$$- \pi a_i^2 \sigma_i \left[\boldsymbol{i} \frac{x_i - x_{i-1}}{l_i} + \boldsymbol{j} \frac{y_i - y_{i-1}}{l_i} + \boldsymbol{k} \frac{z_i - z_{i-1}}{l_i} \right]$$
$$+ \sum_{\substack{j=1,N \\ j \neq i}} \frac{q^2}{R_{ij}^2} \left[\boldsymbol{i} \frac{x_i - x_j}{R_{ij}} + \boldsymbol{j} \frac{y_i - y_j}{R_{ij}} + \boldsymbol{k} \frac{z_i - z_j}{R_{ij}} \right]$$
$$- q \left(\boldsymbol{i} \frac{f_x}{h_x} + \boldsymbol{j} \frac{f_y}{h_y} + \boldsymbol{k} \frac{f_z}{h_z} \right) \tag{7}$$

Through the calculation of the momentum balance of each individual bead, the jet trajectory is simulated and predicted. The calculation process of the jet trajectory model is shown in Fig. 4. During the simulation process, the state information of the first two beads is defined by the initial conditions. When a new bead is added into the system, the state information of each bead is updated in relation to the other N-1 beads. The equations of motion are separated into three directions. These equations are then solved numerically by using ode45 routine in MATLAB. At the beginning of the calculation, the system contains two beads. The state vectors of the first two beads are added to the system as the initial conditions to calculate the dynamics of the beads. In each time-step, the dynamic positions of all the beads in the system are first updated, then two boundary conditions are checked in sequence. First, the position of the furthest bead from the nozzle is checked against zero (collector position). If it reaches the collector, the system vector of that bead is recorded as the deposition location and removed from the system calculation, which means it will no longer influence the dynamics of other beads or be affected by the external electric field. Then, the bead sequence is updated by shifting all the bead index number by one. Second, the boundary condition at the nozzle is evaluated to determine if a new bead will be added to the system. If the latest bead position to the nozzle is greater than one, one new bead is created at the tip of the nozzle. The bead number is added by one in the system vectors and attached to the end of the bead array. Based on the new bead array, the program moves to the next time-step to update the system dynamics again. One
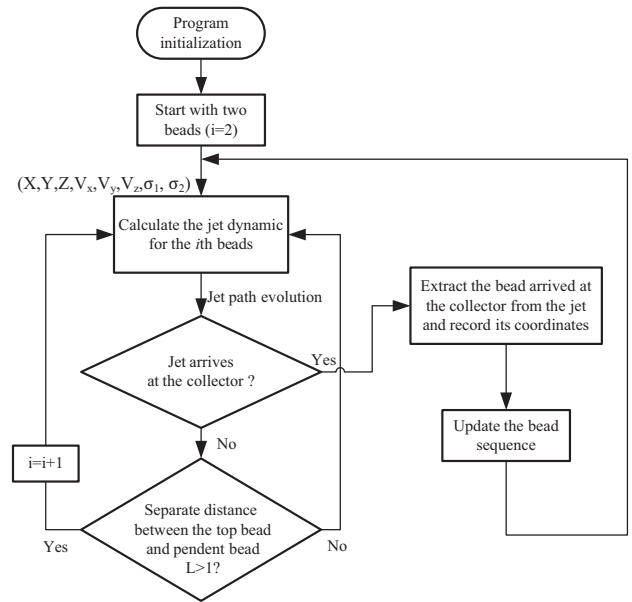
Fig. 4 Calculation flowchart of the proposed jet trajectory model

unique feature of the proposed simulation model is that it takes into accounts the fiber generation and deposition by dynamically adjusting the simulated portion of the electrospinning jet.

Simulation of Jet Trajectories. Two simulation cases are demonstrated here to visualize the development of the jet path during one cycle of oscillation signals. In the first case, a sinusoidal signal of 200 V and 100 Hz is applied to the AEs only in the Y-direction as

$$V_{y1} = 200 \sin 200\pi t \tag{8}$$

In the second case, two sinusoidal signals with a 90-deg phase shift are applied along the X- and Y-directions, respectively, as

$$V_{y2} = 200 \sin 200\pi t \tag{9}$$

$$V_{x2} = 200 \sin \left(200\pi t + \frac{1}{4}\pi \right) \tag{10}$$

Table 1 Parameters used in the computational model

Parameters	Symbol	Value (unit)
Initial jet radius	a	0.015 cm
Initial jet segment length	l	0.00319 cm
Charge	q	8.48 $(g^{1/2}cm^{3/2})$/s
Elastic modulus	G	1×10^6 g/(cm s^2)
Mass	m	0.283×10^{-5} g
Viscosity	μ	1×10^5 g/(cm s)
Density	ρ	1.21×10^{-3} g/cm^3
Applied voltage on nozzle	V_z	2000 V
AE voltage along the X-axis	V_x	200 V
AE voltage along the Y-axis	V_y	200 V
AE signal frequency along the X-axis	ω_x	100 Hz
AE signal frequency along the Y-axis	ω_y	100 Hz
AE signal phase along the X-axis	φ_x	0 degree
AE signal phase along the Y-axis	φ_y	0 degree
Nozzle-to-collector distance	h_z	0.15 cm
Nozzle-to-AE distance in X-axis	h_x	0.12 cm
Nozzle-to-AE distance in Y-axis	h_y	0.12 cm
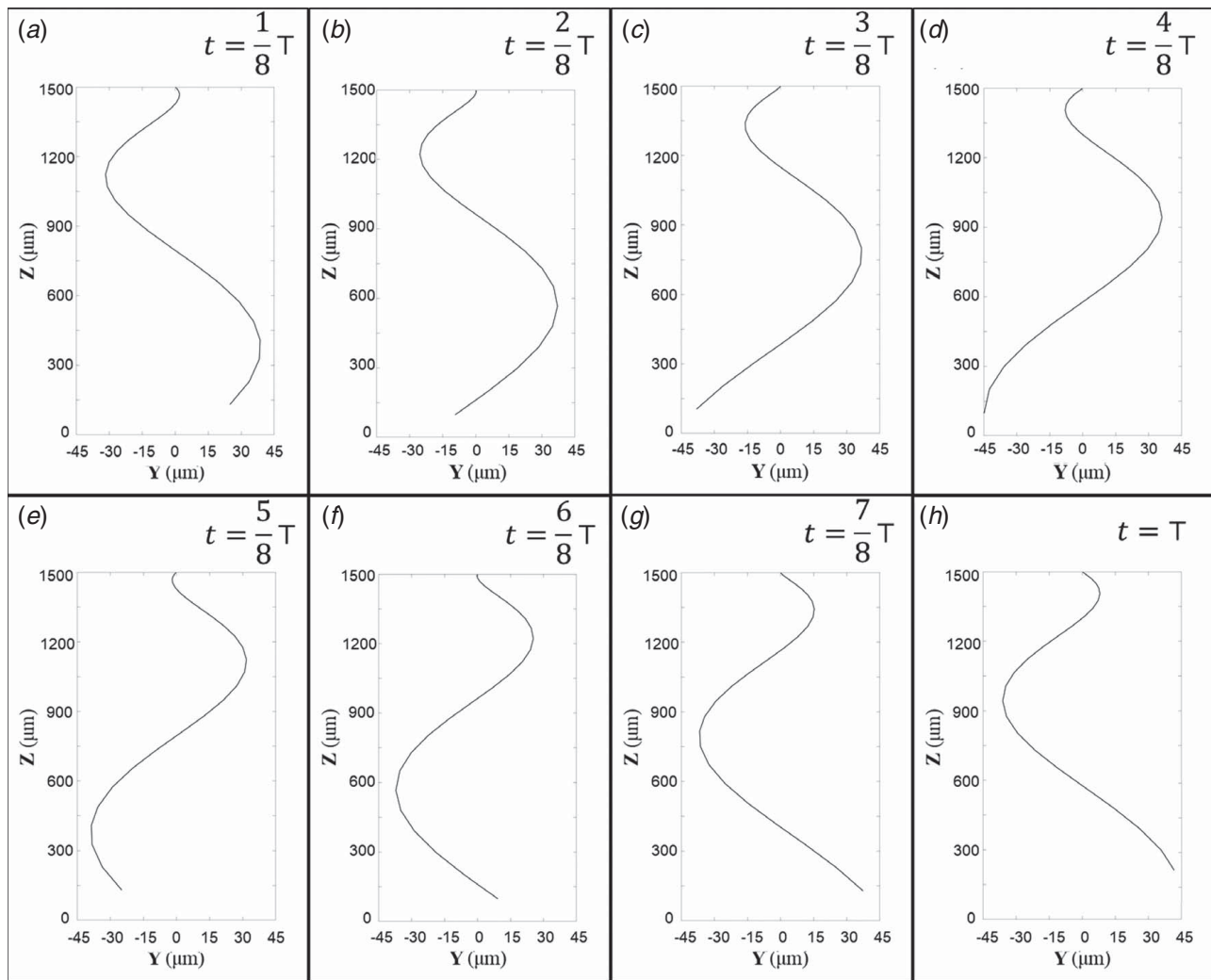
Fig. 5 Trajectory development of a jet path within a cycle with electric signals applied to the auxiliary-electrodes in the Y-direction at (a) $t = \frac{1}{8}T$, (b) $t = \frac{2}{8}T$, (c) $t = \frac{3}{8}T$, (d) $t = \frac{4}{8}T$, (e) $t = \frac{5}{8}T$, (f) $t = \frac{6}{8}T$, (g) $t = \frac{7}{8}T$, and (h) $t = T$

The nozzle-to-collector distance is set at 1.5 mm, while the nozzle-to-AE distance is 1.2 mm. The voltage potential between the nozzle and collector is 2000 V. The collector translation is applied in the X-direction at 10 mm/s. The time increment in the simulation is set at 0.001 s. All the other parameters necessary for the simulation model are summarized in Table 1.

The snapshots of the electrospinning jet at different time instants within a cycle are calculated and plotted in Figs. 5 and 6. The jet fully develops to reach the collector after 29 time-steps of calculation. In case 1, when the external electric field is applied in the Y-direction, as shown in Fig. 5, the movement of the charged jet can be divided into two parts, the longitudinal motion and the lateral motion. Along the longitudinal direction, the charged beads flow continuously from the droplet toward the collector in response to the electrostatic force between the nozzle and the collector. Along the lateral direction, the charged beads oscillate back and forth in response to the electric field established by the externally applied potential on the auxiliary electrodes. It should be emphasized that, at any specific time, not all the segments of the charged jet are swinging in the same direction. Some segments are moving in the positive Y-direction, while the others are in the negative Y-direction. It is due to that the travel time of a bead which starts at the nozzle and ends at the collector is longer than half cycle length, which means that during one period of bead travel time, the direction of lateral electrostatic force will change

more than once, thus causing the charged jet swing to different directions. On the other hand, it is noticed that the amplitude of swing increases with the vertical position of the jet, resulting from the accumulated acceleration time of the traveling beads. In case 2, when the external electric field is applied in the X–Y plane, as shown in Fig. 6, the charged jet is moved in a spiral form, which is driven by the coupled electric forces from the auxiliary electrodes. To achieve a smooth spiral path, two sinusoidal signals with a 90-deg phase shift responding to the actual angle between the adjacent auxiliary electrodes are applied. The arrangement is to guarantee that the direction of the movement of the resultant force in the lateral direction always points to the tangent direction of moving trajectory. During one oscillation cycle, the projection of an arbitrary section in the X–Y planes is always in the form of an ellipse. With the beads moving further and further, the amplitude of ellipse gradually increases.

Experimental Verification. Experimental validation of the theoretical model is carried out by comparing the difference between the experimental results and simulation results, which is used to corroborate the accuracy of the theoretical model. The test setup is schematically shown in Fig. 7 for a modified near-field melt-electrospinning setup. Polycaprolactone (PCL, CAPA 6400, Perstorp Ltd., Warrington, Cheshire, UK), with a molecular weight
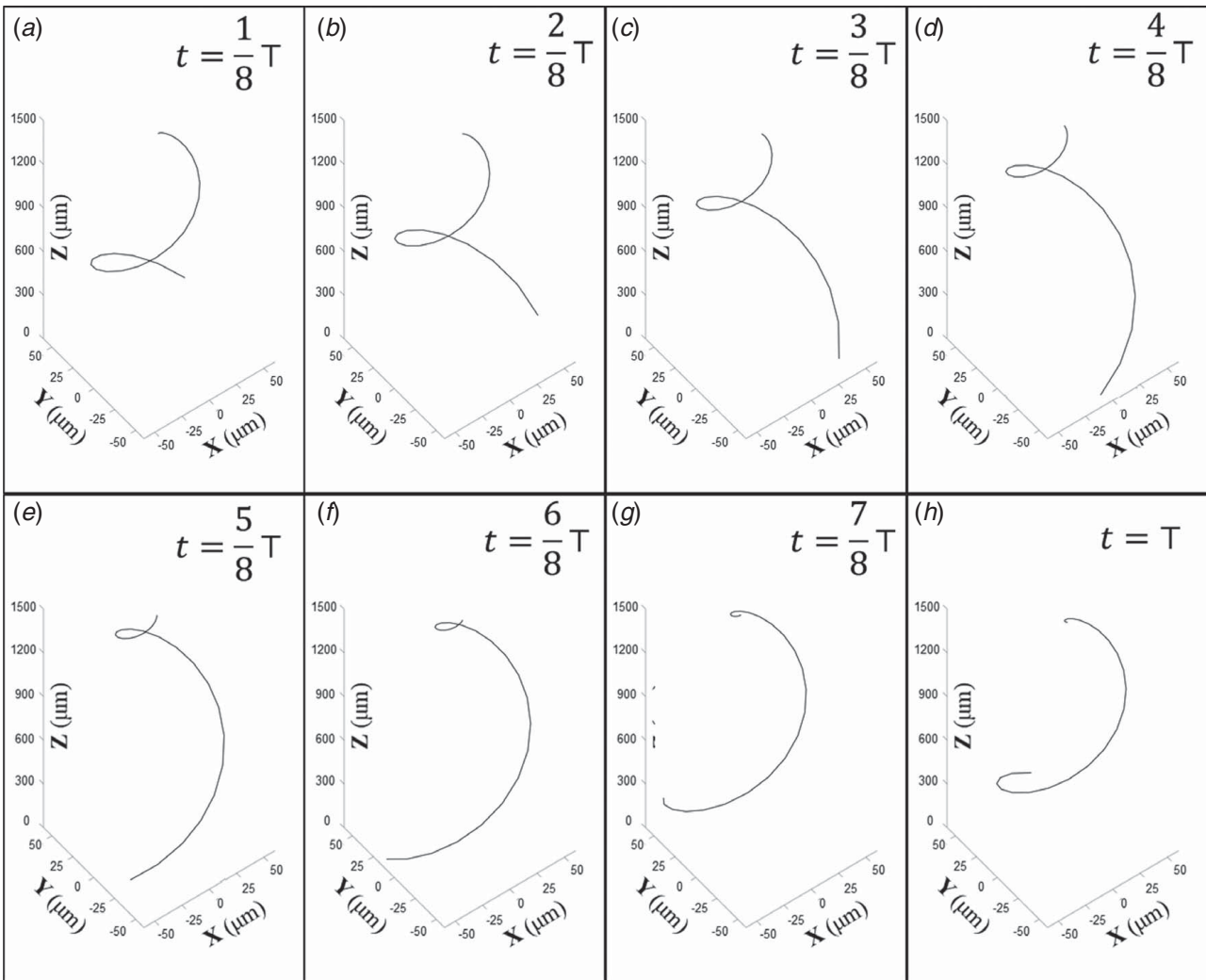
Fig. 6 Trajectory development of a jet path within a cycle with electric signals applied to the auxiliary-electrodes in both *X*- and *Y*-directions at (*a*) at $t=\frac{1}{8}T$, (*b*) $t=\frac{2}{8}T$, (*c*) $t=\frac{3}{8}T$, (*d*) $t=\frac{4}{8}T$, (*e*) $t=\frac{5}{8}T$, (*f*) $t=\frac{6}{8}T$, (*g*) $t=\frac{7}{8}T$, and (*h*) $t=T$

of 50,000 and a melting point of 58 °C is chosen as the stock material for its high thermal stability and good biological properties. A plastic syringe fitted with a metallic needle (gauge 30, inner diameter of 159 μm, and outer diameter of 311 μm) is loaded with PCL beads. A proportional-integral-derivative (PID)-regulated
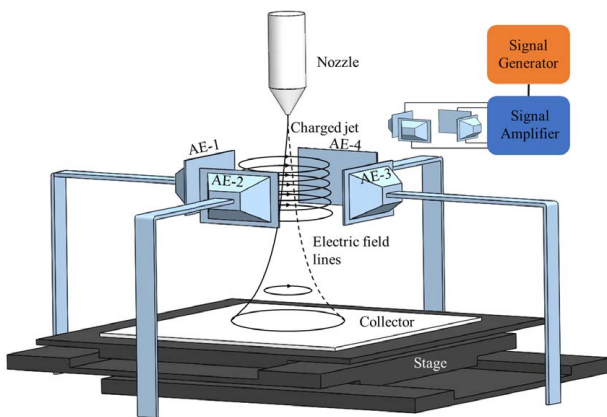
Fig. 7 Schematic illustration of near-field electrospinning platform

electrical heating system is adopted to melt the beads to get the polymer melt. Then, a precision syringe pump (Harvard Apparatus, Remote Infuse/Withdraw PHD Ultra Syringe Pump) is used to control the dispensing of molten polymer. Silicon wafers are used as the collector and mounted on a programmable *X–Y* stages (ALIO Industries, Inc.). Two pairs of auxiliary electrodes made of copper sheets (termed as AE-1, AE-2, AE-3, and AE-4) are fixed around the nozzle. They are not in contact with the motion stage or interfering with its motion. The constant voltage applied to the nozzle is supplied by a high-voltage source (Stanford Research System, Inc.); while the four-channel dynamic signals applied to the side electrodes are generated by a multifunctional data acquisition device (USB-6363, National Instruments, Inc.) and amplified through high-power-voltage amplifiers (PZD 350, TREK, Inc.). The process is monitored and recorded by a microscopic camera (Point Grey Research). The experiment results and fiber geometry are measured using an optical digital microscope (RH-2000, Hirox, Inc.). All the experiments have been carried out at room temperature and atmospheric pressure.

Comparisons between the experimental and calculated fiber patterns are demonstrated in Fig. 8. The experimental parameters used in Figs. 8(*a*) and 8(*c*) are consistent with the simulation parameters used in case 1 and case 2 as mentioned in Sec. 3.2. In the first pair of comparison between Figs. 8(*a*) and 8(*b*), the experimental results are in good agreement with the simulation patterns except for some minor differences such as the irregular waveform, uneven
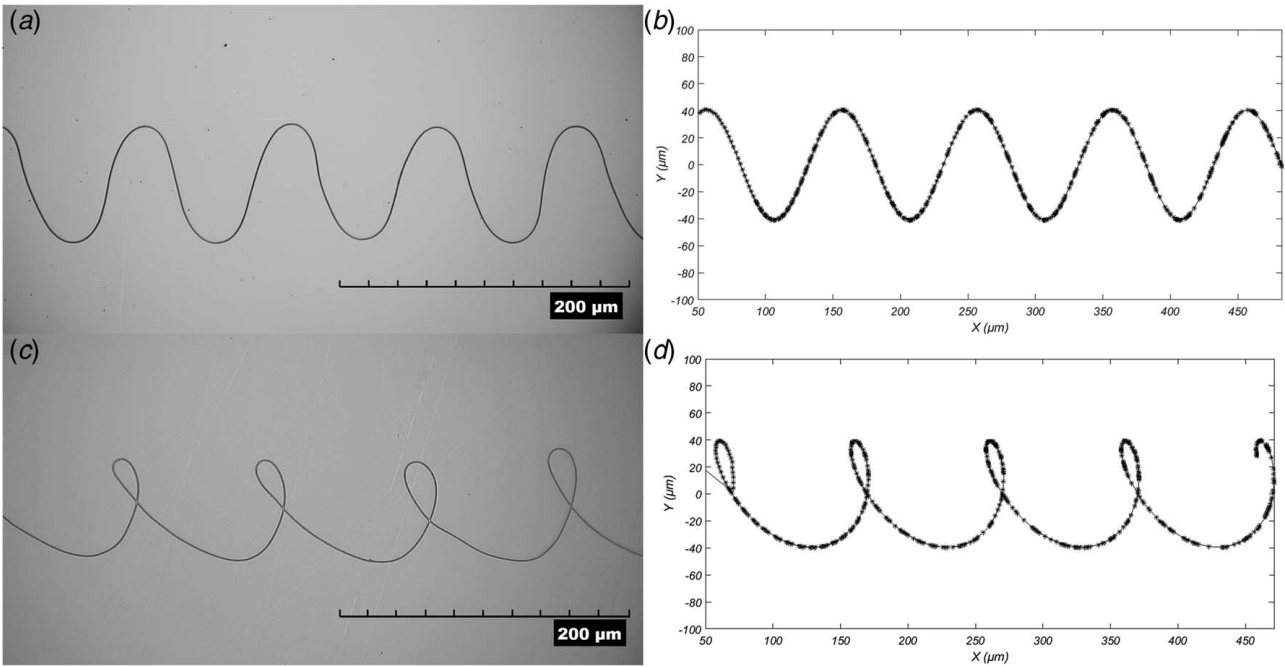
Fig. 8 Comparison between the (a) experimental and (b) calculated fiber patterns corresponding to the simulation case 1; (c) experimental and (d) calculated fiber patterns corresponding to the simulation case 2

amplitude, and wavelength. In the simulation model, the simplification is made to ignore the drag force between the collector and the portion of the jet in touch with the stage, as well as the repulsive force between the residual charges on the collection fibers and the spinning jet. In the actual experimental conditions, though the drag force and residual charge repulsive force are far less than the jet driving force, these forces will cause distortion to the collected patterns as shown in the figure. In addition, the attached dirt and local unevenness of the surface will also induce the irregularity of deposited patterns. In the second pair of comparison between Figs. 8(c) and 8(d), most of the segments are consistent except for the rolling regions where the irregularity of the collected patterns becomes more obvious. It is due to that, at the rolling regions, the large curvature transition causes the viscoelastic force between the arrived segment and upcoming part to be amplified, which prevents the jet to arrive at the intended position. The resistance to bending will, in turn, affect the jet movement, causing the deviation of the jet trajectory. The uncertainty of the dynamic resistance will finally induce the irregularity of the collected patterns. Overall, the experimental results show good agreement with the simulated results. It indicates that the simulation results can be used to guide the deposition process and to predict the fabrication results.

Analysis of the Process Variables

Control Variable Analysis. During the fabrication process, the voltage amplitude of control signals will affect the amplitude of the oscillating jet; the frequency of control signals will affect the velocity of the swing jet; and the applied voltage on the nozzle will affect the fiber diameter, respectively. In this part, the effects of these three control variables on the deposited pattern geometry (amplitude of the deposited structure and fiber diameter) were analyzed through three groups of experiments. The corresponding results are demonstrated in Fig. 9. The default experiment conditions are given as follows: nozzle voltage of 2000 V; AE voltage of a sinusoidal signal of 300 V at 100 Hz; and the collector moving speed of 10 mm/s. The three sets of experiments vary each control variable and are detailed as follows.

In the first group, the voltage amplitude of the applied signal is increased from 150 V to 300 V with a step of 50 V. The deposited wavy patterns are shown in Figs. 9(a)–9(d). The results show that the amplitude of wavy patterns is increased from $30.79 \pm 1.99\ \mu m$ to $75.44 \pm 3.31\ \mu m$ with the corresponding voltage amplitude of the applied signal increased from 150 V to 300 V. With the increase of voltage amplitude on AE, the lateral electrostatic driven force is increased due to the enlarged electric potential, causing the charged jet swing at a larger distance range and generating patterns with an increased amplitude. The experimental results show a positive linear relationship between the two parameters, as shown in Fig. 10(a). The experimental data are in good agreement with the simulation results based on the proposed model. The results show that the amplitude of the wavy patterns depends linearly on the amplitude of AE voltage and can be effectively tuned by changing the amplitude of applied signals.

In the second group, the frequency of the AE signal is varied from 40 Hz to 70 Hz with a step of 10 Hz. As seen from Figs. 9(e)–9(h), the wavelength of deposited structures decreases from $251.14 \pm 4.59\ \mu m$ to $142.51 \pm 2.83\ \mu m$ and the amplitude of wavy patterns decreases from $111.74 \pm 2.83\ \mu m$ to $91.15 \pm 0.92\ \mu m$. A reciprocal relationship between the frequency of the AE signal and the wavelength of deposited structures is revealed and plotted in Fig. 10(b). The correlation between the signal frequency and the pattern amplitude is plotted and shown in Fig. 10(c). All the experimental results are compared with the simulated curves. The experimental results demonstrate a negative linear relationship between the two parameters. The lateral motion acceleration is expected to be proportional to the control signal amplitude, but the distance is affected by both the control signal amplitude and frequency. There is less time for the jet to move in the lateral direction during one oscillation cycle with a higher frequency. Thus, with an identical signal amplitude but a higher frequency, the amplitude of the deposited structure will be decreased. The frequency of the applied signal has a coupled effect on the wavelength and amplitude of the deposited patterns.

In the third group, the applied voltage on the nozzle increased from 2000 V to 2600 V with a step of 200 V. The deposited wavy structures are shown from Figs. 9(i)–9(n). With the increase in the vertical voltage potential from 2000 V to 2600 V, the fiber
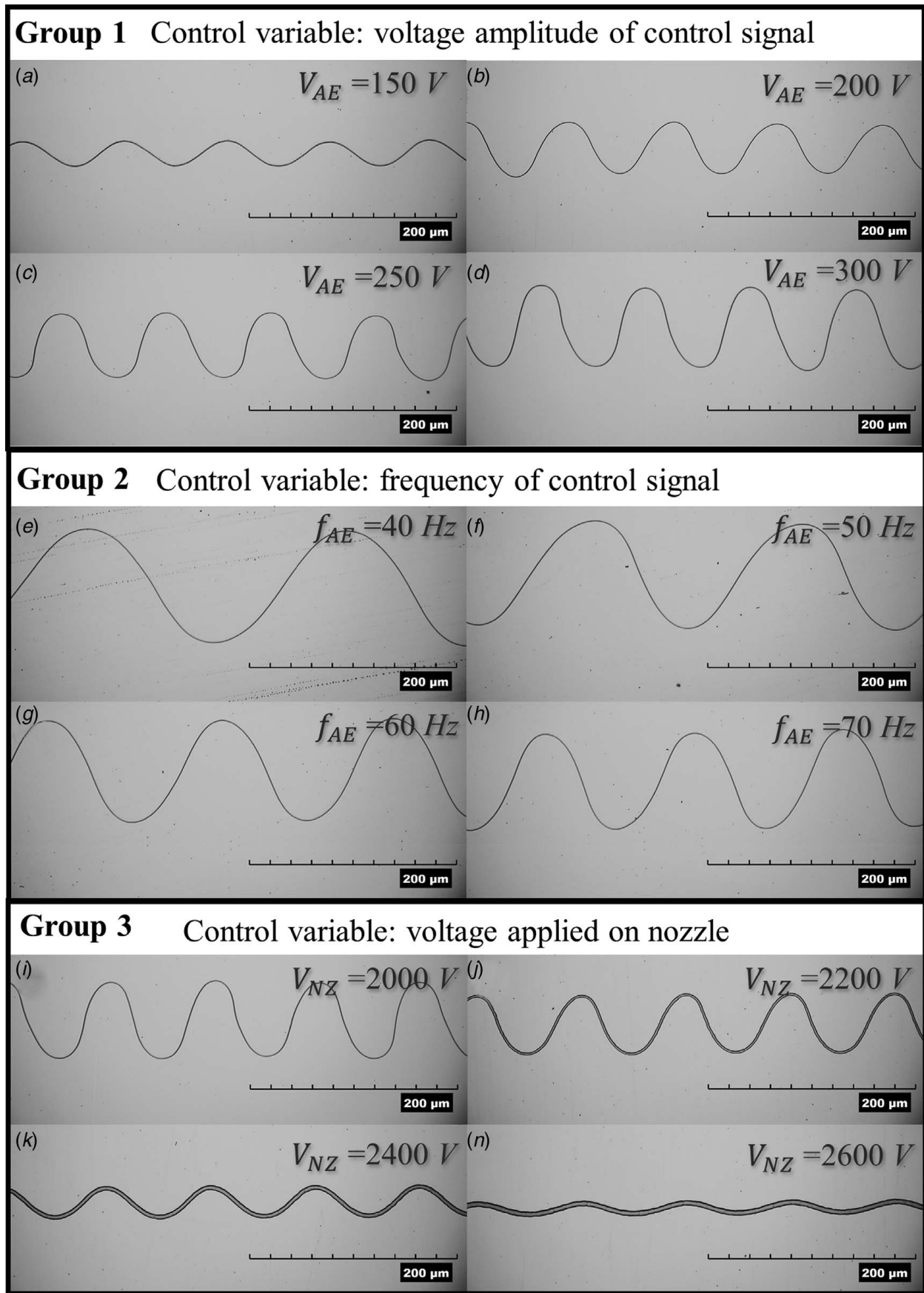
Fig. 9 Experimental results with different experimental parameters: (*a*)–(*d*) deposited wavy patterns with voltage amplitude of the applied signal increased from 150 V to 300 V with a step of 50 V; (*e*)–(*h*) deposited wavy patterns with frequency of the AE signal increased from 40 Hz to 70 Hz with a step of 10 Hz; and (*i*)–(*n*) deposited wavy patterns with applied voltage on nozzle increased from 2000 V to 2600 V with a step of 200 V
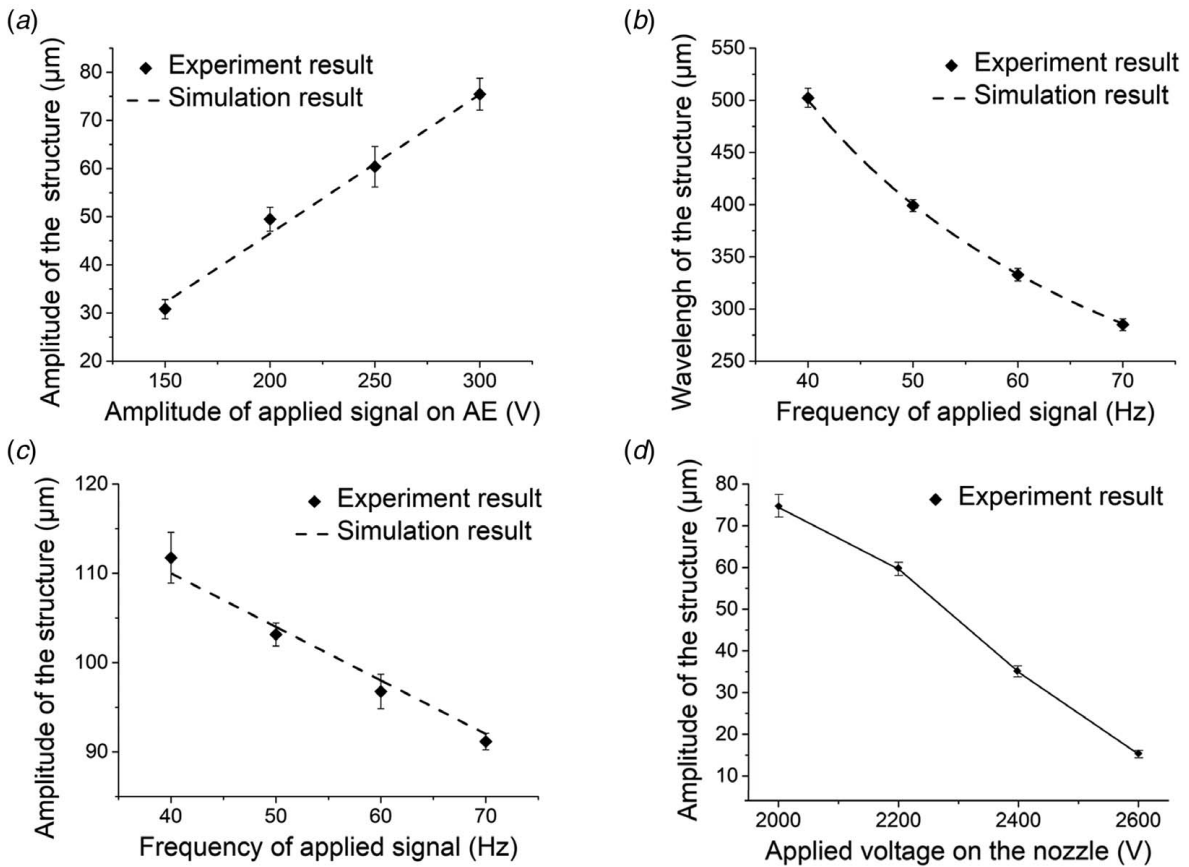
Fig. 10 Relationship between the experimental parameters and structure parameters: (a) relationship between the amplitudes of control signal and patterns; (b) relationship between the signal frequency and structure wavelength; (c) relationship between the signal frequency and structure amplitude; and (d) relationship between the nozzle voltage and structure amplitude

diameter increases from $0.75 \pm 0.01\ \mu m$ to $4.21 \pm 0.08\ \mu m$ and the amplitude of wavy patterns decreases from $75.44 \pm 3.31\ \mu m$ to $15.33 \pm 0.62\ \mu m$. The wavelength of the deposited structure is unchanged when the frequency of AE signals is kept the same. In near-field electrospinning, the larger voltage potential corresponds to the stronger electric force, which leads to the larger volume ejection from the Taylor cone and the increased fiber diameter. Figure 10(d) shows the correlation between the fiber diameter and the deposited structure amplitude. The results show a negative linear relationship between the two parameters. This is due to the fact that the electric charges accumulated on the electrospinning jet are in a first-order relationship with the fiber diameter, while the mass of the jet is in a second-order relationship with the fiber diameter. The increase in fiber diameter will overall decrease its acceleration amplitude in the lateral direction, thus decreasing the pattern amplitude.

Fabrication of Wavy and Coiling Fiber Arrays. To further demonstrate the controllability and capability of the process, complex wavy and coiling fiber arrays with various structure parameters have been fabricated and shown in Fig. 11. The control signals can go beyond simple harmonic oscillations, so the process can be extended to generate arbitrary patterns according to the pre-defined signals. First, two kinds of simple control signals following a sinusoidal function (frequency at 100 Hz and amplitude of 300 V) and a triangular function (frequency at 100 Hz and amplitude of 300 V) are applied in the Y-direction. The voltage applied on the nozzle is 2500 V, and the collector moving speed is 10 mm/s.

The corresponding patterns in the forms of sinusoidal and zig-zag shapes following the control signals are demonstrated in Figs. 11(a) and 11(b). In Fig. 11(c), the applied electric signals consist of the superposition of sinusoidal and triangular functions (frequency at 100 Hz and amplitude of 300 V). In Fig. 11(d), the applied electric signals consist of the superposition of two sinusoidal functions with different amplitudes (amplitude of 300 V and 150 V, respectively) and an identical frequency at 100 Hz. Furthermore, the control signals with two sinusoidal functions are added along both the X- and Y-directions with the amplitude of 300 V and frequency of 100 Hz. The collector translation speed was set at 4 mm/s along the X-direction. Two kinds of coiling patterns with different structural parameters were fabricated and demonstrated. The results showed that the decrease in applied voltage leads to the decrease in fiber diameter and the increase in the pattern amplitude. At last, the capability to produce 3D wavy structures is demonstrated. In Figs. 11(g) and 11(h), sinusoidal voltage signals (frequency at 75 Hz and amplitude of 350 V) were applied to the auxiliary-electrodes in the Y-direction and the stage was controlled to move back and forth in the X-direction at the speed of 10 mm/s. A multi-layer wall structure was built by stacking the wavy patterns. The side view of the fabricated wavy wall structure at the angles of 75 deg and 15 deg is demonstrated. The radius of curvature at the bending part is about $50\ \mu m$, which cannot be produced using the traditional method through purely collector movement. All the above results showed the potential of the proposed approach to actively and reliably control the fiber deposition to fabricate wavy and coiling structures utilizing the additional electrostatic force provided by the auxiliary electrodes.
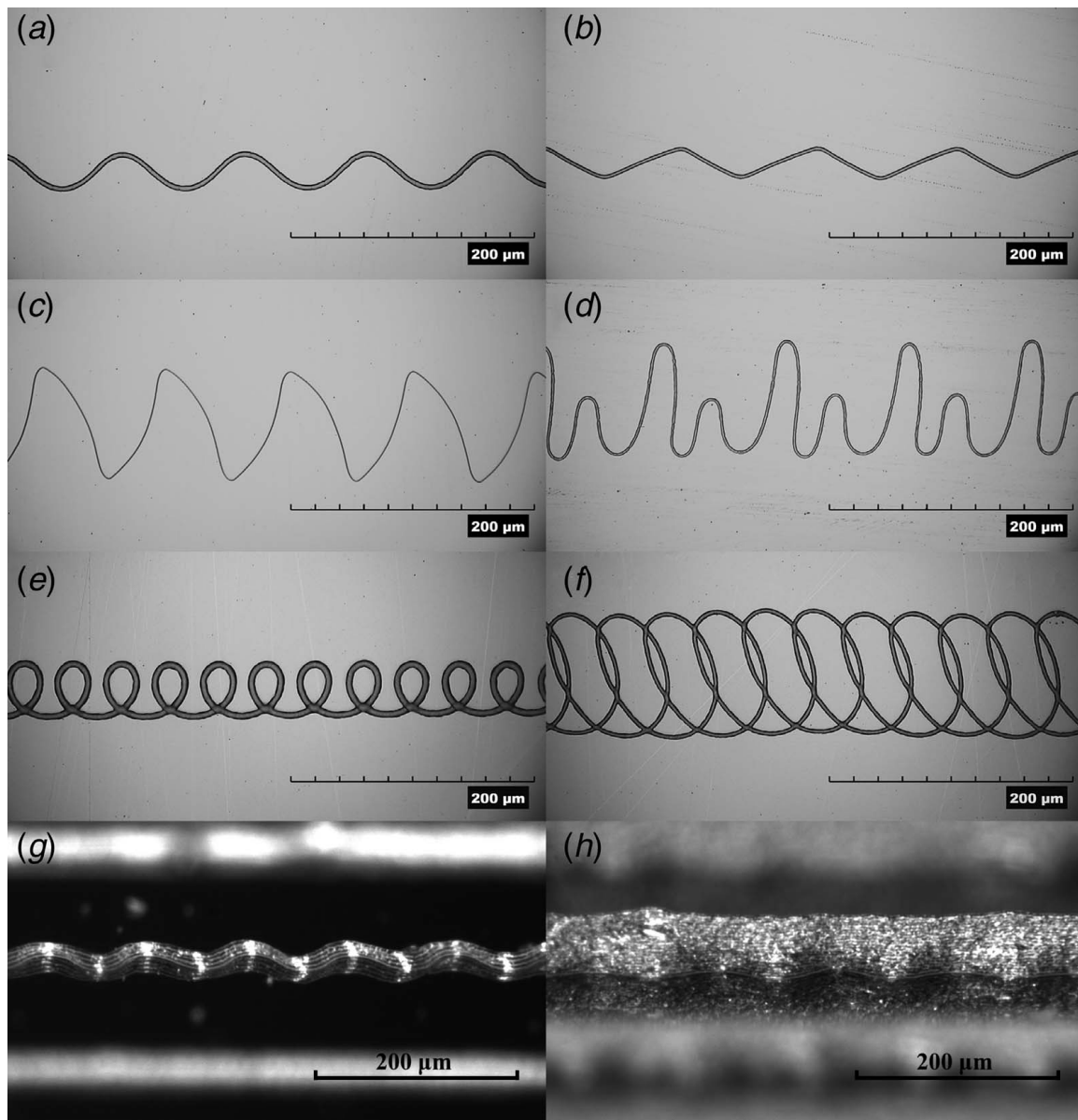
Fig. 11 Wavy and coiling patterns with different structural parameters: (*a*) sinusoidal pattern, (*b*) triangular pattern, (*c*) combination of sinusoidal and triangular pattern, (*d*) combination of two-frequency sinusoidal pattern, (*e*) and (*f*) coiling patterns; side view of the fabricated wavy wall structures in the angle of (*g*) 75 deg, and (*h*) 15 deg

Conclusions

In conclusion, a direct writing process for fabricating wavy and coiling microscale fiber arrays, based on electric field manipulation in NFES, has been developed by introducing active electrostatic signals applied on the side-auxiliary electrodes. By active control of the voltage signals, the structural parameters of the deposited patterns can be easily tuned and controlled. The proposed side-electrode-assisted fabricating method possesses high accuracy and flexible controllability and has overcome the deficiency of traditional electrospinning-based method in generating arbitrary microscale wavy and coiling structures. It is envisioned that this method will benefit the applications in the field of photovoltaic devices, sensors, transducers, resonators, and stretchable electronics. For example, hyper-stretchable self-powered sensors based on buckling-based electrospinning methods were produced with the printed nano/microfibers in the wavy form [29]. The proposed method could be adopted to tune and control patterns in a more consistent and precise manner. Another work demonstrated a wavy-substrate

self-powered sensor by printing the fibers onto a wavy substrate [30]. The fabricated sensor demonstrated the 3D wavy structures have enhanced piezoelectric and electrical performance. The proposed fabrication technique could further simplify the process to directly print wavy fiber structures without using the wavy substrate.

A theoretical model of the modified NFES process with auxiliary electrode signals is constructed to simulate the jet trajectory considering the corresponding forces acting on the electrospinning jet including viscoelastic, charge repulsive, and electric forces. Experimental validation of the model is carried out by comparing the experimental and simulation results. The effects of different process parameters including the voltage amplitude of control signal, voltage frequency of control signal and nozzle-collector voltage on the deposited pattern geometry are analyzed. Wavy and coiling microscale fiber arrays with various structure parameters are successfully fabricated and demonstrated. These results indicate that the deposition of arbitrary wavy and coiling fiber arrays can be precisely and reliably achieved utilizing the proposed side electrode-assisted method in the NFES process.

Acknowledgment

Nomenclature

a = initial jet radius
l = initial jet segment length
m = mass
q = charge
N = total number of beads
G = elastic modulus
h_x = nozzle-to-AE distance in X-axis
h_y = nozzle to AE distance in Y-axis
h_z = nozzle to collector distance
f_E = electric force
f_q = repulsive force
f_{ve} = viscoelastic force
f_x = electric forces along the X-axis
f_y = electric forces along the Y-axis
f_z = electric forces along the Z-axis
V_z = applied voltage on the nozzle
V_x = AE voltage along the X-axis
V_y = AE voltage along the Y-axis
μ = viscosity
ρ = density
φ_x = AE signal phase along the X-axis
φ_y = AE signal phase along the Y-axis
ω_x = AE signal frequency along the X-axis
ω_y = AE signal frequency along the Y-axis

References

[1] Ago, H., Petritsch, K., Shaffer, M. S., Windle, A. H., and Friend, R. H., 1999, "Composites of Carbon Nanotubes and Conjugated Polymers for Photovoltaic Devices," Adv. Mater., 11(15), pp. 1281–1285.
[2] Kong, X. Y., and Wang, Z. L., 2003, "Spontaneous Polarization-Induced Nanohelixes, Nanosprings, and Nanorings of Piezoelectric Nanobelts," Nano Lett., 3(12), pp. 1625–1631.
[3] Zhang, H.-F., Wang, C.-M., Buck, E. C., and Wang, L.-S., 2003, "Synthesis, Characterization, and Manipulation of Helical SiO2 Nanosprings," Nano Lett., 3(5), pp. 577–580.
[4] Huang, Y., Bu, N., Duan, Y., Pan, Y., Liu, H., Yin, Z., and Xiong, Y., 2013, "Electrohydrodynamic Direct-Writing," Nanoscale, 5(24), pp. 12007–12017.
[5] Choi, S. W., Jo, S. M., Lee, W. S., and Kim, Y. R., 2003, "An Electrospun Poly (Vinylidene Fluoride) Nanofibrous Membrane and Its Battery Applications," Adv. Mater., 15(23), pp. 2027–2032.
[6] Beeby, S. P., Torah, R., Tudor, M., Glynne-Jones, P., O'donnell, T., Saha, C., and Roy, S., 2007, "A Micro Electromagnetic Generator for Vibration Energy Harvesting," J. Micromech. Microeng., 17(7), pp. 1257–1265.
[7] Wang, Z. L., and Wu, W., 2012, "Nanotechnology-Enabled Energy Harvesting for Self-Powered Micro-/Nanosystems," Angew. Chem., Int. Ed., 51(47), pp. 11700–11721.
[8] Fang, H.-B., Liu, J.-Q., Xu, Z.-Y., Dong, L., Wang, L., Chen, D., Cai, B.-C., and Liu, Y., 2006, "Fabrication and Performance of MEMS-Based Piezoelectric Power Generator for Vibration Energy Harvesting," Microelectron. J., 37(11), pp. 1280–1284.
[9] Esposito, M., Tasco, V., Todisco, F., Benedetti, A., Sanvitto, D., and Passaseo, A., 2014, "Three Dimensional Chiral Metamaterial Nanospirals in the Visible Range by Vertically Compensated Focused Ion Beam Induced-Deposition," Adv. Opt. Mater., 2(2), pp. 154–161.
[10] Boman, M., Westberg, H., Johansson, S., and Schweitz, J.-A., 1992, "Helical Microstructures Grown by Laser Assisted Chemical Vapor Deposition," Proceedings IEEE Micro Electro Mechanical Systems, Travemunde, Germany, Feb. 4–7, pp. 162–167.
[11] Provin, C., Monneret, S., Le Gall, H., and Corbel, S., 2003, "Three-Dimensional Ceramic Microcomponents Made Using Microstereolithography," Adv. Mater., 15(12), pp. 994–997.
[12] Pham, T. A., Kim, D. P., Lim, T. W., Park, S. H., Yang, D. Y., and Lee, K. S., 2006, "Three-Dimensional SiCN Ceramic Microstructures via Nano-Stereolithography of Inorganic Polymer Photoresists," Adv. Funct. Mater., 16(9), pp. 1235–1241.
[13] Li, D., and Xia, Y., 2004, "Electrospinning of Nanofibers: Reinventing the Wheel?," Adv. Mater., 16(14), pp. 1151–1170.
[14] Dzenis, Y., 2004, "Spinning Continuous Fibers for Nanotechnology," Science, 304(5679), pp. 1917–1919.
[15] Hellmann, C., Belardi, J., Dersch, R., Greiner, A., Wendorff, J. H., and Bahnmüller, S., 2009, "High Precision Deposition Electrospinning of Nanofibers and Nanofiber Nonwovens," Polymer, 50(5), pp. 1197–1205.
[16] Wu, Y., Wu, B., Vijayavenkataraman, S., San Wong, Y., and Fuh, J. Y. H., 2017, "Crimped Fiber With Controllable Patterns Fabricated via Electrohydrodynamic Jet Printing," Mater. Des., 131, pp. 384–393.
[17] Li, D., Wang, Y., and Xia, Y., 2003, "Electrospinning of Polymeric and Ceramic Nanofibers as Uniaxially Aligned Arrays," Nano Lett., 3(8), pp. 1167–1171.
[18] Buttafoco, L., Kolkman, N., Engbers-Buijtenhuijs, P., Poot, A. A., Dijkstra, P. J., Vermes, I., and Feijen, J., 2006, "Electrospinning of Collagen and Elastin for Tissue Engineering Applications," Biomaterials, 27(5), pp. 724–734.
[19] Stankus, J. J., Guan, J., and Wagner, W. R., 2004, "Fabrication of Biodegradable Elastomeric Scaffolds With Sub-Micron Morphologies," J. Biomed. Mater. Res., Part A, 70(4), pp. 603–614.
[20] Kim, G. H., 2006, "Electrospinning Process Using Field-Controllable Electrodes," J. Polym. Sci., Part B: Polym. Phys., 44(10), pp. 1426–1433.
[21] Qin, H., Wei, C., Dong, J., and Lee, Y. S., 2017, "Direct Printing and Electrical Characterization of Conductive Micro-Silver Tracks by Alternating Current-Pulse Modulated Electrohydrodynamic Jet Printing," ASME J. Manuf. Sci. Eng., 139(2), p. 021008.
[22] Deitzel, J. M., Kleinmeyer, J., Hirvonen, J., and Tan, N. B., 2001, "Controlled Deposition of Electrospun Poly (Ethylene Oxide) Fibers," Polymer, 42(19), pp. 8163–8170.
[23] Reneker, D. H., and Yarin, A. L., 2008, "Electrospinning Jets and Polymer Nanofibers," Polymer, 49(10), pp. 2387–2425.
[24] Taylor, G. I., 1964, "Disintegration of Water Drops in an Electric Field," Proc. R. Soc. London, A, 280(1382), pp. 383–397.
[25] Pannier, C. P., Diagne, M., Spiegel, I. A., Hoelzle, D. J., and Barton, K., 2017, "A Dynamical Model of Drop Spreading in Electrohydrodynamic Jet Printing," ASME J. Manuf. Sci. Eng., 139(11), p. 111008.
[26] Tourlomousis, F., Ding, H., Kalyon, D. M., and Chang, R. C., 2017, "Melt Electrospinning Writing Process Guided by a "Printability Number"," ASME J. Manuf. Sci. Eng., 139(8), p. 081004.
[27] Yarin, A. L., Koombhongse, S., and Reneker, D. H., 2001, "Taylor Cone and Jetting From Liquid Droplets in Electrospinning of Nanofibers," J. Appl. Phys., 90(9), pp. 4836–4846.
[28] Reneker, D. H., Yarin, A. L., Fong, H., and Koombhongse, S., 2000, "Bending Instability of Electrically Charged Liquid Jets of Polymer Solutions in Electrospinning," J. Appl. Phys., 87(9), pp. 4531–4547.
[29] Huang, Y., Ding, Y., Bian, J., Su, Y., Zhou, J., Duan, Y., and Yin, Z., 2017, "Hyper-stretchable Self-Powered Sensors Based on Electrohydrodynamically Printed, Self-Similar Piezoelectric Nano/Microfibers," Nano Energy, 40, pp. 432–439.
[30] Fuh, Y. K., Wang, B. S., and Tsai, C. Y., 2017, "Self-Powered Pressure Sensor With Fully Encapsulated 3D Printed Wavy Substrate and Highly-Aligned Piezoelectric Fibers Array," Sci. Rep., 7(1), pp. 1–7.